EDGE ARTICLE

Check for updates

Biomimetically constructing a hypoxia-activated programmable phototheranostics at the molecular level†

Hang Zhang,[a] Jia-Hui Wu,[a] Hao-Zong Xue,[a] Ruijing Zhang,[ab] Zi-Shu Yang,[a] Song Gao [ID][abc] and Jun-Long Zhang [ID]*[ac]

The hypoxic microenvironment is considered the preponderant initiator to trigger a cascade of progression and metastasis of tumors, also being the major obstacle for oxygen consumption therapeutics, including photodynamic therapy (PDT). In this work, we report a programmable strategy at the molecular level to modulate the reciprocal interplay between tumor hypoxia, angiogenesis, and PDT outcomes by reinforcing synergistic action between a H_2O_2 scavenger, O_2 generator and photosensitizer. The modular combination of a catalase biomimetic (tri-manganese cryptand, **1**) and a photosensitizer (Ce6) allowed the rational design of a cascade reaction beginning with dismutation of H_2O_2 to O_2 under hypoxic conditions to enhance photosensitization and finally photooxidation. Concurrently, this led to the decreased expression of the vascular endothelial growth factor (VEGF) and effectively reduced unwanted growth of blood vessels observed in the chick chorioallantois membrane (CAM). Notably, the proof-of-principle experiments using the tumor-bearing models proved successful in enhancing PDT efficacy, prolonging their life cycles, and improving immunity, which could be monitored by magnetic resonance imaging (MRI).

Introduction

Many advances in therapeutics and diagnostics have often emerged from the causation of a specific biological function to individual molecular events, especially when our prior knowledge is sketchy. Over the last decade, as the understanding of biology has increased exponentially, it is now recognized that biology, specifically behind cancer, is extraordinarily complex. It primarily arises from the complex, dynamic interaction known as the tumor microenvironment (TME), involving multiple cellular components and chemical clues such as the pH, oxygen level, *etc.*[1–3] As a result, scientists can start to think of designing smart medicines such as autonomous machines that can be programmed by regulating the traditional treatments and the molecular hallmarks of the TME.[4–8] To precisely perform a therapeutic intervention, diagnosis, or theranostics that combines both, constructing such combination medicines

at the molecular level is highly desirable, but how to choose the appropriate components to achieve synergistic action remains unclear. In this work, we reported a "proof-of-concept" design of programmable phototheranostics to conduct a cascade hypoxia-activated photodynamic therapy (PDT) and angiogenesis (Scheme 1).
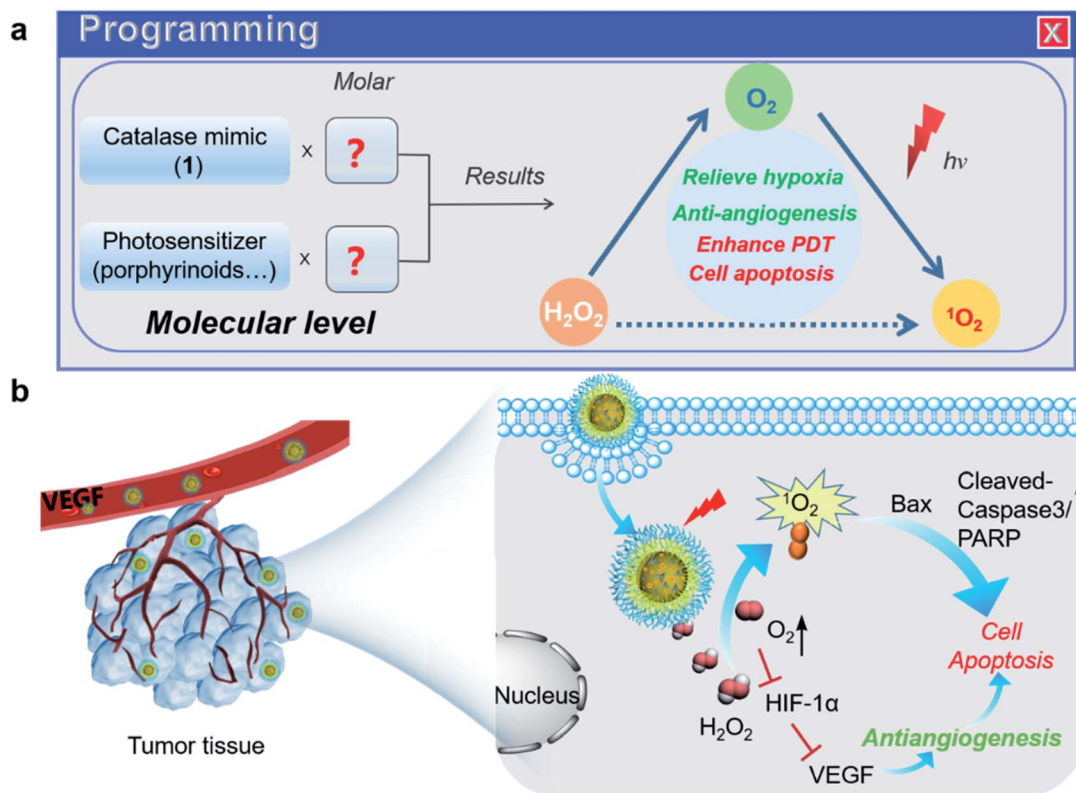
Hypoxia, a pathological condition where the partial oxygen pressure is lower than 10 mm Hg, is the hallmark of the TME originating from abnormal redox metabolism in tumors.[9,10] The hypoxic TME often leads to the accumulation of hydrogen peroxide (H_2O_2) as the major metabolic intermediate that triggers downstream angiogenic factors in tumor cells, promotes angiogenesis to restore oxygen and nutrient supply, and ultimately affects tumor proliferation, metastases, and immunity.[11–17] Thus, the hypoxic TME is considered the preponderant initiator in these cascade events and becomes an important target for anticancer therapies, especially oxygen-dependent treatments. On the other hand, PDT is a prominent treatment highly dependent on the local oxygen concentration in tumor sites, which can be photosensitized to a singlet oxygen and thus destroy cancerous cells upon light irradiation of a photosensitizer (PS).[18–22] Despite encouraging therapeutic efficacy, tumor hypoxia is disadvantageous to PDT, and the subsequent PDT-induced oxygen consumption triggers or even exacerbates angiogenesis, which is known to affect treatments negatively.[23] Therefore, the reciprocal interplay between the hypoxic TME,

[a] Beijing National Laboratory for Molecular Sciences, College of Chemistry and Molecular Engineering, Peking University, Beijing 100871, P. R. China. E-mail: zhangjunlong@pku.edu.cn

[b] Guangdong-Hong Kong-Macao Joint Laboratory of Optoelectronic and Magnetic Functional Materials, Spin-X Institute, School of Chemistry and Chemical Engineering, South China University of Technology, Guangzhou 510641, P. R. China

[c] Chemistry and Chemical Engineering Guangdong Laboratory, Shantou 515031, China

Scheme 1 Programmable phototheranostics. (a) Schematic illustration of programmable phototheranostics containing a catalase mimic and photosensitizer. (b) The proposed synergistic mechanism of PDT combined with anti-angiogenesis for dealing with hypoxia of the tumor environment.

angiogenesis, and PDT provides the underlying guideline for designing programmable medicines.[24,25]

To relieve tumor hypoxia, increasing the oxygen levels of tumors has been demonstrated to enhance the sensibility of hypoxic tumors toward PDT.[26] In contrast to the direct use of oxygen carriers such as perfluorocarbon carbide materials or oxygen precursors, including endoperoxides,[27–29] the regulation of the hypoxic TME *via* continuously generating O_2 *in vivo* has attracted increasing attention.[30–38] Such a metabolic shift allows the implementation of a "one stone two birds" strategy that effectively alleviates oxidative stress to dictate the anti-angiogenic response and improve PDT efficacy.[39,40] Metal oxide nanoparticles that performed the catalase-like dismutation of H_2O_2 have been extensively explored as chemodynamic catalysts for this purpose.[41–43] Direct use of antioxidant enzymes such as catalase has also been reported; however, the obstacles, including large molecular weight, high expense, low cellular uptake, and easy hydrolytic degradation by the proteases in living cells, need to be overcome.[44,45] To maximize the synergistic action of different ingredients, design of such a combination medicine at the molecular level would be particularly desirable. Thus, it remains of interest to use a molecular H_2O_2 scavenger by virtue of small molecular size, reproducible preparation, enzyme-like catalytic efficiency and quantitative integrability. The present work was motivated by an appreciation that the catalase mimics salen-based tri-manganese

cryptands catalytically dismute H_2O_2 and treat oxidative stress-related disorders, potentially acting as a molecular inhibitor for angiogenesis.[46–49] We also noticed that such Mn-based complexes are attractive magnetic resonance imaging (MRI) agents due to their high-spin electronic configuration. Thus, they possess the capability of noninvasive imaging or diagnostics that yields molecular target information before, during, and after cognate therapy.[50,51]

To maximize the synergy, integrating the PS and the tri-Mn (salen) complex into a nanoplatform using 1,2-distearoyl-*sn*-*glycero*-3-phosphoethanolamine-*N*-[methoxy(polyethylene glycol)] (DSPE-PEG2000) allows the cascade reaction comprising dismutation of intracellular H_2O_2 and photosensitization of down-stream O_2, in a biomimetic manner to naturally occurring photosynthetic systems.[52] Here, we were inspired to couple the photosensitizers with biomimetic synthetic structures for the catalase center (tri-manganese) *via* self-assembling,[46] facilitating attainment of natural photosynthesis processes.[52] More importantly, the synergism we achieved in the artificial photosynthetic system can significantly improve the reactive efficiency in some oxidations toward cholesterol and unsaturated fatty acids by a singlet oxygen. Compared to the metal oxide nanoparticles that have been extensively demonstrated in chemotherapy, the synergic action of combination phototheranostics described here can be modulated by rationally tuning the ratio of the ingredients, including the PS and

catalytic center at the molecular level, representing one of the features of this work. After optimization, the most effective system inhibits the formation of new blood vessels and enhances $^1O_2$ production and thus improves PDT efficacy, as demonstrated by *in vitro/in vivo* experiments. Given the importance of the redox metabolic shift on reshaping PDT efficacy, this work provides a programmable strategy to design novel phototheranostics, enhancing tumor treatment and potentially reducing the risk of tumor resistance and recurrence.

Results and discussion

Preparation of programmable phototheranostics

As a result of our continued interest in exploring the biomedical applications of catalase biomimetic complexes,[46] we found that C_3 symmetric salen-based tri-manganese cryptands have the capability of scavenging intracellular ROS, thus potentially relieving hypoxia of the TME.[53] In this work, we chose tri-Mn (salen) cryptand (**1**) with an *o*-diaminobenzene moiety, which displayed the highest reactivity toward H_2O_2 dismutation among our previously reported Mn compounds. We obtained a single crystal of **1** suitable for X-ray diffraction in the mixed methanol/ethanol solution (v/v = 1 : 1) and first confirmed the connectivity of the C_3 symmetric Mn (salen) cryptand (CCDC: 2159529†). Fig. 1b and Table S1† show that **1** has a triple-axis passing through two methyl carbon atoms. The distances between the bridgehead carbon atoms and metal centers were 5.83 and 6.20 Å. The dimensions of the triangular prism cage-like cavity surrounded by six oxygens of phenoxy are 2.76 Å in height and 4.01 Å in each triangular side length, similar to those in previously reported C_3 symmetric Zn (salen) cryptands.[54]
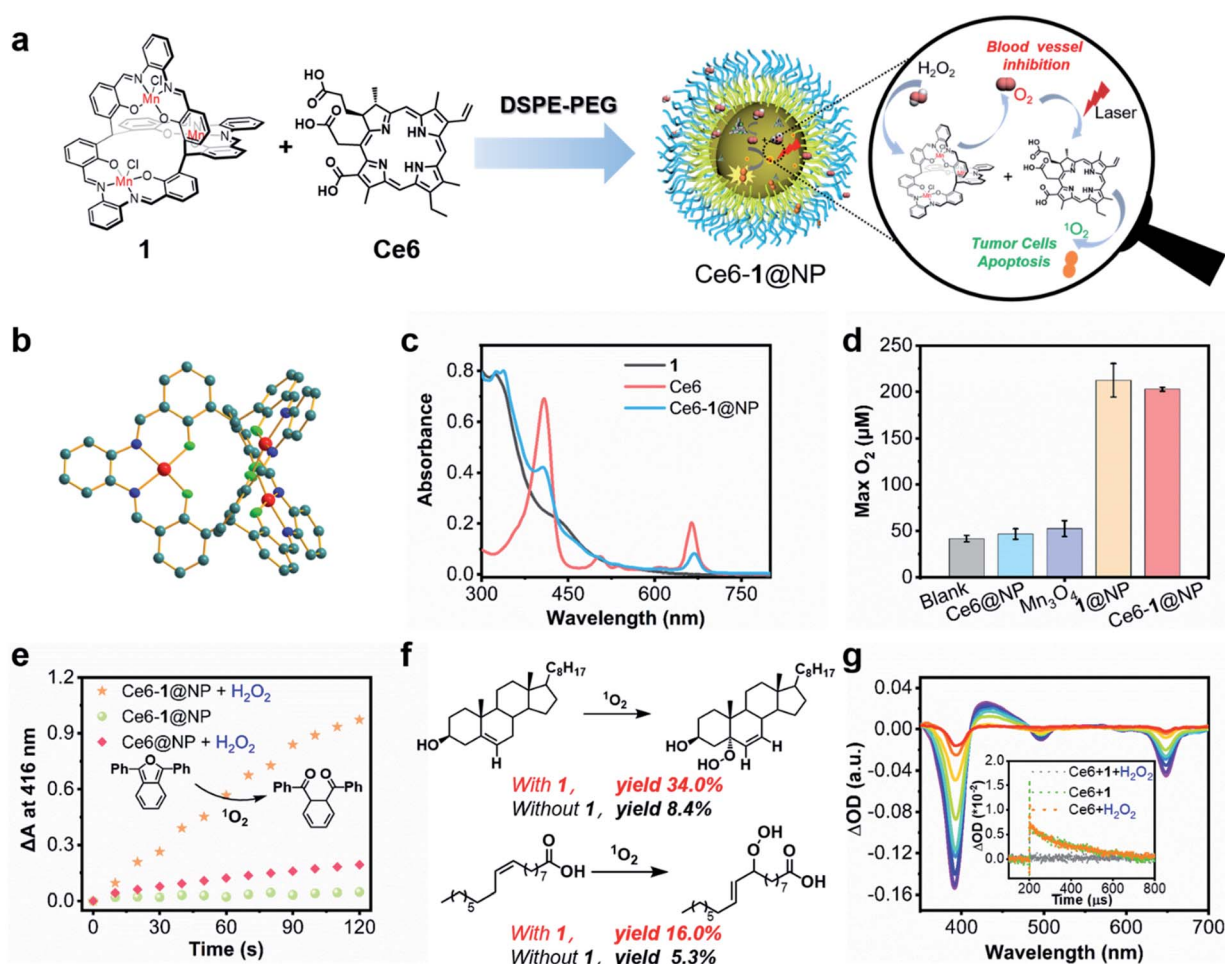

Fig. 1 Preparation and reactivity of phototheranostics. (a) Schematic diagram of Ce6-1@NP synergistically catalyzing H_2O_2. (b) X-ray crystal structure of **1**; hydrogen atoms, solvents, and chloride anions are omitted for clarity. (c) UV-vis spectra of **1**, Ce6 and Ce6-1@NP. (d) Oxygen production *via* catalytic dismutation of H_2O_2 (100 mM) by Ce6@NP, **1**@NP, Mn$_3$O$_4$, and Ce6-1@NP (5 μM) in PBS buffer (pH 7.4). (e) The ability of Ce6@NP (with 10 mM H_2O_2), Ce6-1@NP (with 10 mM H_2O_2) and Ce6-1@NP to promote singlet oxygen generation under hypoxic conditions; the absorbance of DPBF at 416 nm was recorded every 10 s upon red light irradiation (660 nm, 6.5 mW cm^{-2}). (f) Photooxidation activities. Cholesterol (20 mg) or oleic acid (20 mg); catalyst (Ce6, 0.25 mg), **1** (1 mg), H_2O_2 (30%, 40 μL), MeCN/CHCl$_3$/H$_2$O (1 mL/1 mL/200 μL), N$_2$ bubbling, 50 mW cm^{-2} 660 nm LED. (g) Transient absorption difference spectra of Ce6 measured at selected times in water (0–2000 μs); the inset shows the decay traces of "Ce6+1 with H_2O_2", "Ce6+1" and "Ce6 with H_2O_2" in water recorded under a nitrogen atmosphere (Ce6: 15 μM; H_2O_2: 10 mM).

We used DSPE-PEG (MW. 2000), a United States Food and Drug Administration approved amphiphilic phospholipid polymer conjugate,[55] as a biocompatible nanocarrier which may prolong blood circulation time, improve stability and enhance encapsulation efficiency (Fig. 1a).[56] The phototheranostic agent termed Ce6-1@NP was prepared with 1, Ce6, and DSPE-PEG, and the concentrations of 1 and Ce6 were estimated by the absorbances at 325 nm and 665 nm (Fig. 1c) according to their extinction coefficients. The as-prepared phototheranostic agent possessed a spherical morphology with a radius of ca. 100 nm determined by transmission electron microscopy and with a hydrodynamic diameter of ca. 70 nm recorded by dynamic light scattering experiments (Fig. S1 and S2†). We also used the commercial Mn_3O_4 nanomaterial as a control to replace 1 at the same molar mass according to chemical formular. Dismutation of H_2O_2 was examined in PBS buffer (100.0 mM, pH 7.4). As shown in Fig. 1d and S3a, we observed the formation of 217.2 μM and 204.9 μM oxygen in the presence of 5.0 μM 1 and Ce6-1@NP in 400 s, respectively. Only 50.0 μM O_2 in 400 s was obtained by Mn_3O_4, in which the active site may be only at the surface of nanoparticles exposed to aqueous media. Importantly, we conducted this experiment for evaluating the pH effect on producing oxygen catalyzed by Ce6-1@NP. The results were shown in Fig. S3b–d.† Upon increasing pH from 3.0 to 9.0, the yields of oxygen enhanced and exhibited a pH-dependence. When pH was lower than 3.0, Ce6-1@NP almost lost the reactivity toward dismutation of H_2O_2.

We used 1,3-diphenylisobenzofuran (DPBF) to probe $^1O_2$ generation according to the absorption intensity (DA) at 416 nm (Fig. 1e and S4†).[58] For Ce6-1@NP under an N_2 atmosphere, direct irradiation at 660 nm could not trigger $^1O_2$ production, while in the presence of H_2O_2 (10 mM), high yield of $^1O_2$ ($\Delta A \sim 0.97$) was obtained (Fig. S4†). Similar irradiation of the controls, either 1@NP or Ce6@NP with H_2O_2, gave low yields of $^1O_2$ ($\Delta A < 0.2$), probably arising from light-induced self-decomposition of H_2O_2. Nanosecond transient absorption spectroscopy was performed to monitor the triplet excited states of Ce6 in deaerated water.[59] As shown in Fig. 1g, Ce6 (15 μM) displayed negative absorption centered at 390 nm and 655 nm that was ascribed to the ground state bleaching, accompanied by the appearance of positive absorption with the maximum at 460 nm. The lifetime for the triplet state was ca. 141.2 μs, irrelevant to whether 1 (7.5 μM) existed or not. However, in the presence of 1, H_2O_2 addition led to dramatic quenching of the triplet state of Ce6 and a shortening of the lifetime to 0.22 μs, much less than that in the control experiment in the absence of 1. This strongly suggests that 1 catalyzed H_2O_2 dismutation could be the oxygen source under hypoxic conditions for further photooxidation.

Since $^1O_2$ is generally considered the critical ROS in PDT to oxidize biomolecules such as proteins, nucleic acids, or lipids, we chose cholesterol and oleic acid as the examples to test the activity of Ce6-1@NP in the presence of H_2O_2 under an N_2 atmosphere.[60–62] As shown in Fig. 1f and S5,† yields of 16% and 34% of 5a-hydroperoxycholesterol and peroxyl oleic acid were obtained, respectively, ca. 4 times higher than those obtained by the control Ce6@NP. These results again highlighted the

critical role of 1 in reprogramming the redox TME that acts both as an H_2O_2 scavenger and as an O_2 generator.

In addition, we examined the longitudinal relaxivity (r_1) for Ce6-1@NP, which displayed a larger r_1 of 39.2 mM^{-1} s^{-1} than 1 (12.3 mM^{-1} s^{-1}), probably for its encapsulation inside DSPE-PEG (Fig. S6†). With the potential as an MRI contrast agent, Ce6-1@NP thus holds promise to act as a programmable phototheranostic agent that monitors the PDT response and prognosis estimation process by non-invasive MRI imaging.

Synergistic action *in vitro*

A characteristic of programmable medicine is the quantitative integrability of active ingredients to synergistically exert optimum therapeutic efficiency. Toward this goal, we carried out a preliminary study to optimize the synergism of Ce6 and 1 at the molecular level in order to maximize $^1O_2$ production in the presence of H_2O_2 (10 mM) under hypoxic conditions. For example, when the concentration of Ce6 was fixed to 5 μM, we changed the concentration of 1 (5–50 μM) and found the highest yield of $^1O_2$ ($\Delta A \sim 0.63$) when the ratio of Ce6 to 1 was 1 : 6, as shown in Fig. 2a and S7.†

Next, we optimized the ratio of Ce6 vs. 1 in Ce6-1@NP according to the photocytotoxicity against HeLa cells. The synergistic effect was evaluated according to the synergy index (SID), where SID = $(C_a/S_a) + (C_b/S_b)$ is as shown in Table S2.†[63]
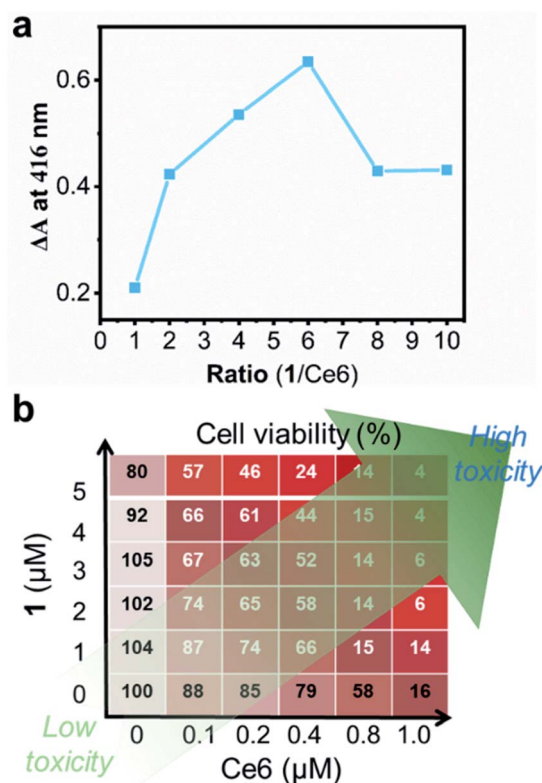

Fig. 2 Synergistic action of Ce6 and 1. (a) Singlet oxygen generation with 1 of different ratios (5–50 μM) under hypoxic conditions detected by DPBF assay. (b) Synergy index (SID, SID = $(C_a/S_a) + (C_b/S_b)$) for photocytotoxicity in HeLa cells under hypoxic conditions.[63]

SID_{50} (0.72) and SID_{arb} (0.69) were smaller than 1.0, suggestive of the synergistic effect in Ce6-1@NP. SID_{50} and SID_{arb} represented the SIDs when the inhibition of cells reached 50% and the arbitrary level, respectively. Fig. 2b shows that Ce6-1@NP with the ratio of Ce6 to 1 of 1 : 4 showed the best synergistic effect in living cells and would be used in the context. Here, we optimized the ratio of Ce6 to 1 in solution, and the concentration range of 1 is 5–50 μM, and the results showed that the ratio is 1 to 6 when the yield of the singlet oxygen reaches the highest. The difference in the ratios of 1 and Ce6 between living cells and the solution lied in their distinct physical conditions. For example, the distribution of Ce6 or 1 was not homogeneous as that in the solution. Moreover, when 1 was used in high concentrations, the dark cytotoxicity was obvious (Fig. S9†). In order to avoid ambiguous experimental results, we lowered the concentration of 1 to a relatively safe concentration (1 μM) and thus obtained an optimal ratio of Ce6 to 1 of 1 to 4 in living cells. Therefore, we assumed that the difference between living cells and the solution was a possible reason for the difference in the optimal ratio of 1 to Ce6 we observed in living cells and the solution. Of course, we could not exclude the possibility that there may be other factors that contributed to the different ratios of Ce6 to 1. Nonetheless, in this context, we performed the cytotoxicity assay using the optimized Ce6-1@NP under hypoxic or normoxic conditions in HeLa cells. Under normoxic and no light conditions, IC_{50}s values of Ce6@NP and Ce6-1@NP were *ca.* 3.0−5.0 μM (Fig. S8†), while they were decreased to 0.06 μM and 0.04 μM upon light irradiation (660 nm, 30 mW cm^{-2}, 1 min), respectively (Fig. S9 and S10†). A comparison of their photocytotoxicity indicated that the PDT effect was mainly dependent on Ce6, not 1, under normoxic conditions.

Interestingly, the cell-cultured plate sealed in an Anaero-Pouch-Bag for 6 hours was used to simulate hypoxic conditions;[64] the photocytotoxicity of Ce6@NP and Ce6-1@NP decreased, evidenced by the increasing IC_{50}s of 0.36 μM and 0.22 μM in the absence of H_2O_2 (Fig. 3a), suggesting the importance of oxygen for PDT efficacy. When 4.0 μM external H_2O_2 was added to the hypoxic cell culture media, Ce6-1@NP showed an IC_{50} of 0.07 μM, a *ca.* 3-fold decrease of IC_{50} (0.22 μM) of Ce6@NP (Fig. 3b). To verify the effect of H_2O_2, we used the glutathione peroxidase 4 inhibitor (RSL3) to trigger endogenous H_2O_2 accumulation under the hypoxic conditions.[65] As shown in Fig. S11 and S12,† Ce6-1@NP still displayed a decreased IC_{50} of 0.03 μM, while Ce6@NP only showed a slightly decreased IC_{50} of *ca.* 0.11 μM. These results suggested that, in the presence of 1, either endogenous or exogenous H_2O_2 might act as oxygen suppliers that could be subsequently converted to $^1O_2$ in Ce6-1@NP, which showed the synergistic validity.

To investigate the cell death signaling pathway, we used western blotting to evaluate the expression levels of Bax, cleaved caspase-3, and cleaved PARP, the apoptotic marker proteins in HeLa cells (Fig. S13†). In the absence of light irradiation, Ce6-1@NP exhibited similar expression levels of such proteins to the control group, while under light irradiation, it led to a *ca.* 10–30 fold up-regulating of Bax, cleaved PARP, and cleaved caspase 3 when compared with the control group (Fig. S13†). Since 1@NP-*hν* did not show cytotoxicity toward HeLa cells, we did not carry
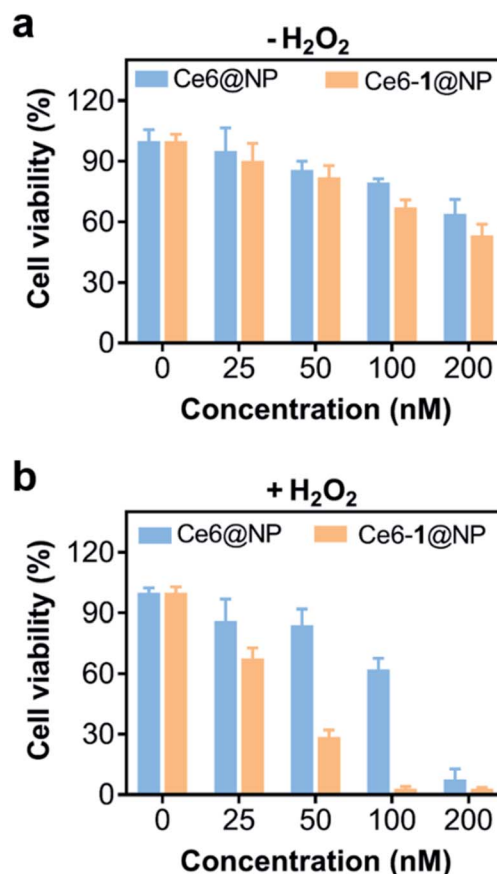

Fig. 3 The cytotoxicity of Ce6@NP and Ce6-1@NP. (a) Under hypoxic conditions without external H_2O_2. (b) Under hypoxia with external H_2O_2 (4 μM); irradiation conditions: 660 nm, 30 mW cm^{-2}, 1 min.

out the western blot experiments for the group of 1@NP-*hν*. The results for comparison of 1, Ce6, and Ce6-1 are listed in Fig. S13b,† and the second group of columns "Ce6-1@NP" contained the effects of 1 in the absence of light irradiation, among which Ce6 has no PDT effect without light irradiation. Within the concentration range used in this part of the experiments, Ce6 (200 nM) did not show any cytotoxicity in the absence of light irradiation (Fig. S8†), and 1 (800 nM) did not show any cytotoxicity in the presence of light irradiation (Fig. S9†). The expression of Bcl-2 was kept unchanged for all groups. These results indicated that mitochondrial-mediated apoptosis might be involved.[66]

Anti-angiogenesis study

We then examined the effect of Ce6-1@NP and Ce6@NP on the expression of HIF-1α, a master regulator of cellular homeostatic response to hypoxia as well as the VEGF that is critical to controlling the pro-angiogenic activity in HUVEC cells.[67,68] As shown in Fig. 4a and b, Ce6-1@NP combined with light irradiation decreased the expression of both HIF-1α and the VEGF, similar to the control groups Ce6-1@NP (in the dark) and Ce6@NP. To further investigate the inhibition of angiogenesis, we constructed a CAM model to evaluate drug efficacy,[69] and the whole treatment is shown in Fig. 4d. Axitinib, a commercially
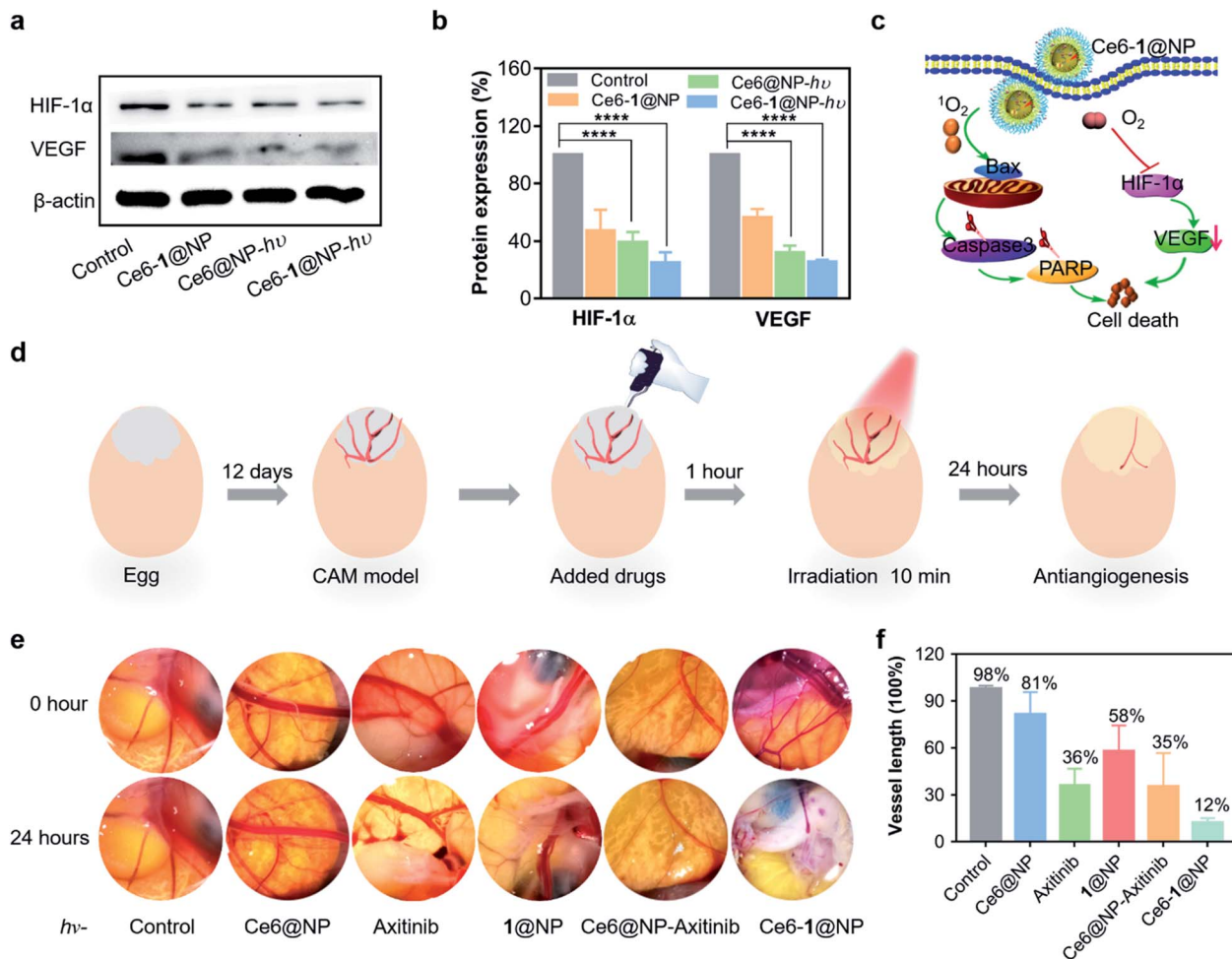
Fig. 4 Anti-angiogenesis studies. (a) Western blot analysis and (b) statistical analysis for expression levels of the VEGF and HIF-1α. (c) Schematic diagram of the cell death mechanism induced by Ce6-1@NP under laser irradiation. (d) Protocol for anti-angiogenesis in the CAM model. (e) Photos of anti-angiogenesis in the CAM model with different groups (control, Ce6@NP, Axitinib, 1@NP, Ce6@NP–Axitinib and Ce6-1@NP; 660 nm, 30 mW cm^{-2}, 10 min, 4 μM based on Ce6 content). (f) Statistical analysis for the vessel length of different groups. The results are presented as mean ± SD. *$p < 0.05$ and **$p < 0.01$ as compared with the control group.

available VEGF receptor known to inhibit angiogenesis, was chosen as a positive control to prepare the Ce6@NP–Axitinib protocol.[70]

Through the window that was carefully created on the top-most surface of an eggshell, 100 μL Ce6-1@NP or Ce6@NP (containing 4 μM Ce6 and 16 μM 1) or 1@NP (16 μM) or Axitinib (16 μM) or "Ce6@NP + Axitinib" was added to the CAM vascular bed. After 1 hour incubation, all eggs were exposed to light (660 nm, 30 mW cm^{-2}, 10 min). Fig. 4e shows inhibition of angiogenesis after different treatments, and the efficacy was estimated from the vessel length. Upon treatment with Ce6-1@NP, the vascular ruptured, and the vessel length was reduced by 88%. Less significant inhibition of angiogenesis was observed in "Ce6@NP + Axititib", 1@NP, Axitinib, and Ce6@NP groups, with vessel lengths reduced by 65%, 42%, 64%, and 19%, respectively (Fig. 4f). Thus, Ce6-1@NP displays more effective anti-angiogenesis compared to Ce6@NP and Axitinib, demonstrating the synergistic validity of the photo-synthetic cascade protocol.

These results suggested that Ce6-1@NP not only exhibited high photocytotoxicity but also inhibited the expression of HIF-1α and the VEGF, which shows the potential for anti-angiogenesis. On the basis of these results, we proposed the synergistic mechanism of 1 and PS, as shown in Fig. 4c. 1 catalyzes the dismutation of endogenous H_2O_2, which improves hypoxia and thus prevents tumor angiogenesis by inhibiting the expression of HIF-1α and the VEGF, to produce oxygen that can be photosensitized to a singlet oxygen and destroy tumor cells upon irradiation of PSs.

Antitumor efficacy *in vivo*

In view of a synergistic effect of Ce6-1@NP, we further explored the therapeutic efficacy on HeLa tumor-bearing BALB/c female nude mice. Then the mice bearing tumors that were about 100 mm^3 were treated with Ce6-1@NP, Ce6@NP–Axitinib, Axitinib, 1@NP, or Ce6@NP, respectively ($n = 4$; Ce6 was 1 mg kg^{-1}, 1 was 8.4 mg kg^{-1}, and Axitinib was 2.6 mg kg^{-1}) through intra-venous administration, and the mice were irradiated with

a 660 nm laser at a power density of 0.2 W cm^{-2} for 10 min. The tumor volumes were measured on the following 14 days with a Vernier caliper every 2 days[71] (Fig. 5a). As depicted in Fig. 5d, the control (PBS), 1@NP-$h\nu$, and Axitinib-$h\nu$ groups exhibited the neglectable inhibition of tumor growth, further illustrated by the corresponding photographs in Fig. 5e and the mean tumor weights (Fig. S14†) after all mice were harvested. Interestingly, the Ce6-1@NP group under light irradiation exhibited the most significant inhibition among all groups. The tumor

growth rate treated with Ce6-1@NP was slower (ca. 46.7% of the control) than that of Ce6@NP (ca. 69.1% of the control), suggesting that 1 enhances the PDT effect of Ce6. However, the Ce6@NP–Axitinib group showed a similar therapeutic effect (72.4%) on Ce6@NP. Importantly, Ce6-1@NP can monitor the accumulation behavior *in vivo* through MR imaging, and a tumor-to-normal (T/N) contrast ratio of up to 210% was observed for 24 hours (Fig. 5b and c), indicating that Ce6-1@NP can be accumulated in the tumors. Thus, these *in vivo* results
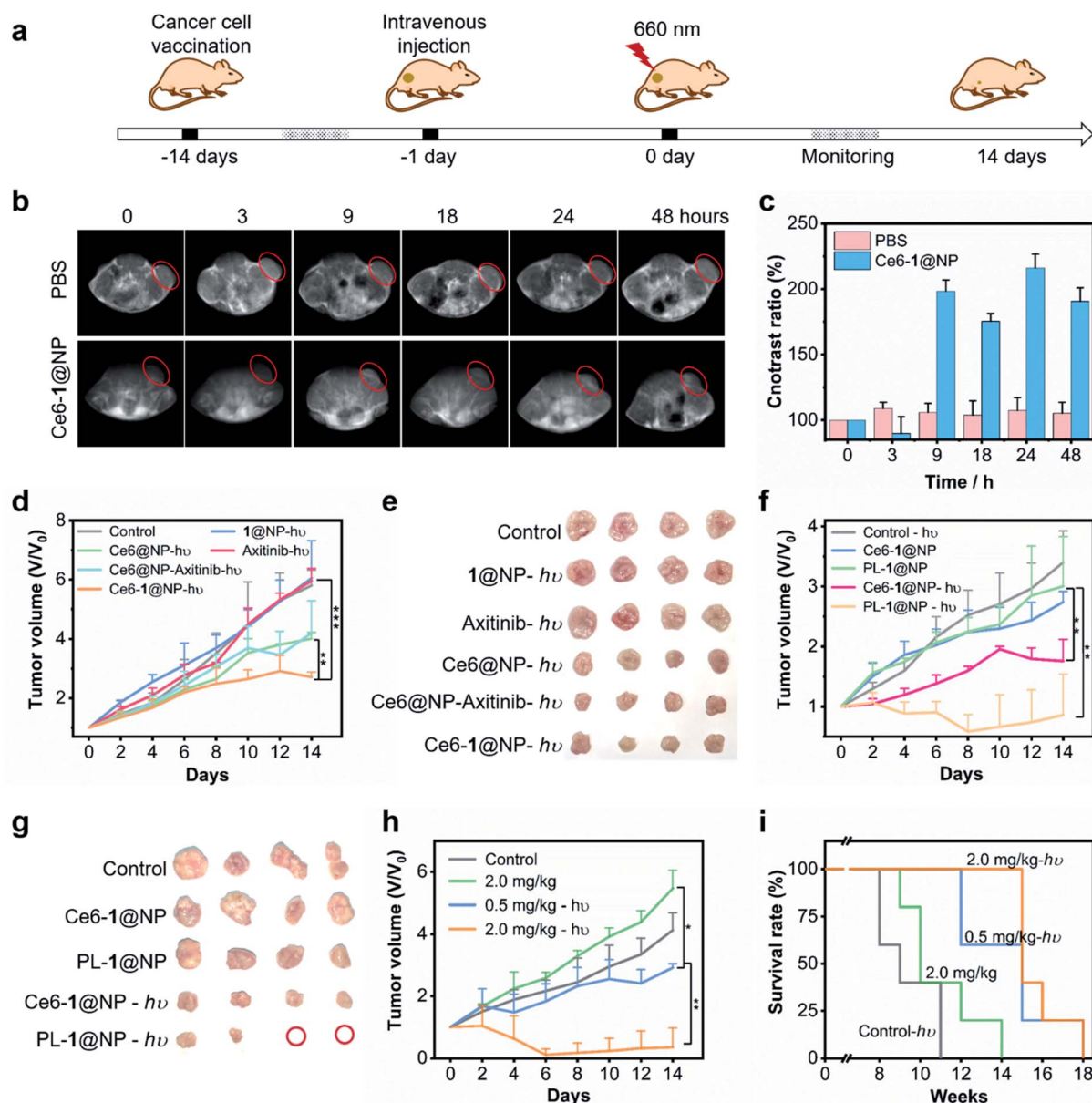

Fig. 5 Antitumor effects on nude mice *in vivo*. (a) Schematic illustration of the antitumor process in mice, 0.2 W cm^{-2} for 10 min with 660 nm light. (b) MR imaging of the mice injected with Ce6-1@NP and PBS. (c) The tumor-to-normal (T/N) contrast ratio in MR imaging. (d, e) The tumor volume curves and digital photographs for the mice treated with different groups (control, 1@NP-$h\nu$, Axitinib-$h\nu$, Ce6@NP-$h\nu$, Ce6@NP–Axitinib-$h\nu$ and Ce6-1@NP-$h\nu$; 1 mg kg^{-1} based on Ce6 content). (f, g) The tumor volume curves and digital photographs for the mice treated with different groups (control, Ce6-1@NP, PL-1@NP, Ce6-1@NP-$h\nu$ and PL-1@NP-$h\nu$; 1 mg kg^{-1} based on Ce6/PL content). (h) The tumor volume curves for the mice treated with different concentration groups (control, 0.5 mg kg^{-1} PL-1@NP-$h\nu$, 2 mg kg^{-1} PL-1@NP and 2 mg kg^{-1} PL-1@NP-$h\nu$; 0.5 or 2 mg kg^{-1} based on PL content). (i) The survival curves of mice treated with different groups. The results are presented as mean ± SD. *$p < 0.05$ and **$p < 0.01$ as compared with the control group.
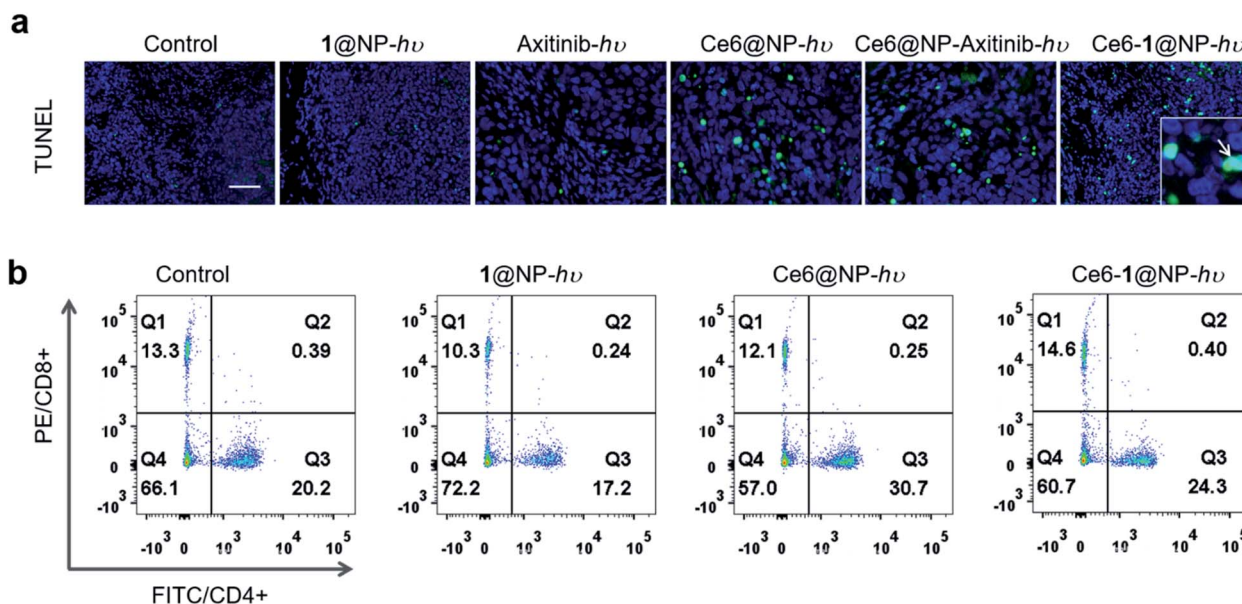
Fig. 6 Apoptosis and immunity *in vivo*. (a) Analysis of tumor cell apoptosis by TUNEL assay for different groups (control, **1**@NP-*hv*, Axitinib-*hv*, Ce6@NP-*hv*, Ce6@NP−Axitinib-*hv*, and Ce6-**1**@NP-*hv*); scale bar = 100 μm. (b) Flow cytometry analysis of CD4+/CD8+ T lymphocytes in B16 tumor-bearing mice for different groups (control, **1**@NP-*hv*, Ce6@NP-*hv*, and Ce6-**1**@NP-*hv*).

demonstrated that Ce6-**1**@NP was an effective phototheranostic agent that combines PDT therapy and MRI imaging modalities.

Further, terminal deoxynucleotidyl transferase-mediated dUTP nick-end labeling (TUNEL) assay of tumor sections (Fig. 6a) revealed a significant increase of apoptotic cells in the Ce6-**1**@NP-*hv* group.[72] Immunohistochemical analysis showed that the expressions of Bax and cleaved caspase 3 were up-regulated. The VEGF expression was decreased after the treatment with Ce6-**1**@NP (Fig. S15†), suggesting that the combination of Ce6 and catalase biomimetic **1** could activate the apoptosis pathway and anti-angiogenesis *in vivo*. Additionally, the body weights (Fig. S16†) and hematoxylin and eosin (H&E) staining for main organs (the heart, liver, spleen, lung, and kidney) indicated that there was no significant tissue damage or apparent histopathological abnormalities or lesions observed in all groups (Fig. S17†).

As mentioned, hypoxia could lead to high expression of the VEGF and then induce tumor angiogenesis. Previous research has demonstrated that vascular injury could activate the immune system and increase immunotoxic T cells, which are necessary against tumors.[16,17] We next analyzed the spleen T lymphocytes to evaluate the system immunity. Fig. 6b shows that the Ce6-**1**@NP could increase the percentage of CD4+/CD8+ cells in the spleen of B16 tumor-bearing mice (40.9%), while the proportion of the control group is 33.5%, **1**@NP group 27.5%, and Ce6-**1**@NP group 42.8%. These results suggested that Ce6-**1**@NP remarkably increased antitumor immunity of mice compared with the control groups.

In order to better improve the therapeutic outcomes, we used the tertrapentafluorophenylporpholactol (PL) that emerged as a chlorophyll type photosensitizer with high singlet oxygen quantum yield[73] to replace Ce6 and prepared a new PL-**1**@NP phototheranostic agent. Fig. 5f shows that PL-**1**@NP is much

more efficient than Ce6-**1**@NP with the reduced tumor sizes of 24.0% and 48.9% respectively, under the same dose (1 mg kg^{-1}), consistent with the results of the mean weight of tumors in Fig. S18† and the tumor photographs in Fig. 5g after the mice were harvested. Subsequently, we conducted a series of dose-dependent experiments as shown in Fig. 5h, and the therapeutic effect was significantly improved with increasing amount of PL-**1**@NP. Importantly, the survival times of the mice treated with PL-**1**@NP (2 mg kg^{-1}) were maximally prolonged to 4–7 weeks compared with the controls, which were treated with PBS (Fig. 5i). Replaceability of different photosensitizers shows improved therapeutic efficacy, revealing the feasibility and expansibility of such a combination strategy.

Conclusions

In summary, we constructed a "programmable photo-theranostics" consisting of tri-manganese metal cryptand **1** and a PS (Ce6 or PL) to trigger the cascade reaction of the dismutation of intracellular H_2O_2 and downstream photosensitization of O_2, allowing the synergistic action of PDT and anti-angiogenesis. Importantly, using the molecular PS and catalase-like H_2O_2 scavenger, the efficiency, more accurately, the synergistic effect could be modulated by quantitative manipulation of the proportion of the two active ingredients (**1** and PS). This is a step closer to programmable medicine. Other than excellent performance in *in vitro* and *in vivo* PDT treatments, this phototheranostic agent showed the effectiveness in inhibition of new blood vessels in the CAM model, in the line with the western blotting for the hypoxia and vascular endothelial growth factor-related proteins (HIF-1α and VEGF). These results revealed a pathway to achieve synergistic PDT with anti-angiogenesis especially using a biomimetic model compound,

which is prospective to further design programmable medicine at the molecular level.

Data availability

All experimental data and procedures are provided in the manuscript and supplementary information (ESI).†

Author contributions

Conceptualization: H. Z., J.-H. W., H.-Z. X., R. J. Z., Z.-S. Y., S. G. and J.-L. Z. Data curation: H. Z., J.-H. W., H.-Z. X., R. J. Z. and Z.-S. Y. Investigation: H. Z., J.-H. W., and J.-L. Z. Project administration: H. Z. and J.-L. Z. Writing – original draft: H. Z. and J.-L. Z. Writing – review & editing: H. Z., S. G. and J.-L. Z. Funding acquisition: S. G. and J.-L. Z. Supervision: J.-L. Z.

Conflicts of interest

There are no conflicts to declare.

Acknowledgements

References

1 J. Jin, M. Ovais and C. Y. Chen, *Nano Today*, 2018, **22**, 83–99.

2 Y. L. Wan, L. H. Fu, C. Y. Li, J. Lin and P. Huang, *Adv. Mater.*, 2021, **33**, 2103978.

3 B. Kumar, A. K. Adebayo, M. Prasad, M. L. Capitano, R. Z. Wang, P. Bhat-Nakshatri, M. Anjanappa, E. Simpson, D. J. Chen, Y. L. Liu, J. M. Schilder, A. B. Colter, C. Maguire, C. J. Temm, G. Sandusky, E. H. Doud, A. B. Wijeratne, A. L. Mosley, H. E. Broxmeyer and H. Nakshatri, *Sci. Adv.*, 2022, **8**, eabh3375.

4 X. F. Ji, R. T. Wu, L. L. Long, X. S. Ke, C. X. Guo, Y. J. Ghang, V. M. Lynch, F. H. Huang and J. L. Sessler, *Adv. Mater.*, 2018, **30**, 1705480.

5 X. F. Ji, Z. Li, X. L. Liu, H. Q. Peng, F. Y. Song, J. Qi, J. W. Y. Lam, L. L. Long, J. L. Sessler and B. Z. Tang, *Adv. Mater.*, 2019, **31**, 1902365.

6 Z. M. Tang, Y. Y. Liu, D. L. Ni, J. J. Zhou, M. Zhang, P. R. Zhao, B. Lv, H. Wang, D. Y. Jin and W. B. Bu, *Adv. Mater.*, 2020, **32**, 1904011.

7 Z. J. Gu, S. Zhu, L. Yan, F. Zhao and Y. L. Zhao, *Adv. Mater.*, 2019, **31**, 1800662.

8 P. H. Zhang, D. Gao, K. L. An, Q. Shen, C. Wang, Y. C. Zhang, X. S. Pan, X. G. Chen, Y. F. Lyv, C. Cui, T. X. Z. Liang, X. M. Duan, J. Liu, T. L. Yang, X. X. Hu, J. J. Zhu, F. Xu and W. H. Tan, *Nat. Chem.*, 2020, **12**, 381–390.

9 T. Q. Duong, C. Ladecola and S. G. Kim, *Magn. Reson. Med.*, 2001, **45**, 61–70.

10 H. E. Williams, V. C. Loades, M. Claybourn and D. M. Murphy, *Anal. Chem.*, 2006, **78**, 604–608.

11 W. H. Xu, M. M. S. Lee, J. J. Nie, Z. H. Zhang, R. T. K. Kwok, J. W. Y. Lam, F. J. Xu, D. Wang and B. Tang, *Angew. Chem., Int. Ed.*, 2020, **59**, 9610–9616.

12 A. Weiss, H. van den Bergh, A. W. Griffioen and P. Nowak-Sliwinska, *Biochim. Biophys. Acta, Rev. Cancer*, 2012, **1826**, 53–70.

13 H. Min, J. Wang, Y. Q. Qi, Y. L. Zhang, X. X. Han, Y. Xu, J. C. Xu, Y. Li, L. Chen, K. M. Cheng, G. N. Liu, N. Yang, Y. Y. Li and G. J. Nie, *Adv. Mater.*, 2019, **31**, 1808200.

14 R. J. Gillies, D. Verduzco and R. A. Gatenby, *Nat. Rev. Cancer*, 2012, **12**, 487–493.

15 T. P. Szatrowski and C. F. Nathan, *Cancer Res*, 1991, **51**, 794–798.

16 M. Zhou, X. Y. Wang, S. C. Lin, Y. F. Liu, J. S. Lin, B. Jiang, X. Z. Zhao and H. Wei, *Adv. Ther.*, 2021, **4**, 2000191.

17 A. S. Jassar, E. Suzuki, V. Kapoor, J. Sun, M. B. Silverberg, L. M. Cheung, M. D. Burdick, R. M. Strieter, L. M. Ching, L. R. Kaiser and S. M. Albelda, *Cancer Res*, 2005, **65**, 11752–11761.

18 K. Y. Ni, G. X. Lan, S. S. Veroneau, X. P. Duan, Y. Song and W. B. Lin, *Nat. Commun.*, 2018, **9**, 4321.

19 M. L. Li, Y. J. Shao, J. H. Kim, Z. J. Pu, X. Z. Zhao, H. Q. Huang, T. Xiong, Y. Kang, G. Z. Li, K. Shao, J. L. Fan, J. W. Foley, J. S. Kim and X. J. Peng, *J. Am. Chem. Soc.*, 2020, **142**, 5380–5388.

20 L. Z. Gao, J. Zhuang, L. Nie, J. B. Zhang, Y. Zhang, G. Ning, T. H. Wang, J. Feng, D. L. Yang, S. Perrett and X. Y. Yan, *Nat. Nanotechnol.*, 2007, **2**, 577–583.

21 D. W. Jiang, D. L. Ni, T. Zachary, P. Huang, X. Y. Yan and W. B. Cai, *Chem. Soc. Rev.*, 2019, **48**, 3683–3704.

22 Y. G. Li, P. Sun, L. Y. Zhao, X. H. Yan, K. P. N. Dennis and P. C. Lo, *Angew. Chem., Int. Ed.*, 2020, **59**, 23228–23238.

23 Y. L. Dai, C. Xu, X. L. Sun and X. Y. Chen, *Chem. Soc. Rev.*, 2017, **46**, 3830–3852.

24 K. J. Liu, H. L. Yao, Y. Wen, H. Zhao, N. J. Zhou, S. L. Lei and L. Xiong, *Biochim. Biophys. Acta, Mol. Basis Dis.*, 2018, **1864**, 2871–2880.

25 Y. J. Li, H. Sui, C. L. Jiang, S. M. Li, Y. Han, P. Huang, X. X. Du, J. W. Du and Y. X. Bai, *Cell. Physiol. Biochem.*, 2018, **48**, 2035–2045.

26 H. S. Jung, J. Han, H. Shi, S. Koo, H. Singh, H. J. Kim, J. L. Sessler, J. Y. Lee, J. H. Kim and J. S. Kim, *J. Am. Chem. Soc.*, 2017, **139**, 7595–7602.

27 W. Fudickar and T. Linker, *Angew. Chem., Int. Ed.*, 2018, **57**, 12971–12975.

28 G. S. Song, C. Liang, X. Yi, Q. Zhao, L. Cheng, K. Yang and Z. A. Liu, *Adv. Mater.*, 2016, **28**, 2716–2723.

29 Y. H. Cheng, H. Cheng, C. X. Jiang, X. F. Qiu, K. K. Wang, W. Huan, A. Yuan, J. H. Wu and Y. Q. Hu, *Nat. Commun.*, 2015, **6**, 8785.

30 Y. Yang, M. Chen, B. Z. Wang, P. Wang, Y. C. Liu, Y. Zhao, K. Li, G. S. Song, X. B. Zhang and W. H. Tan, *Angew. Chem., Int. Ed.*, 2019, **58**, 15069–15075.

31 Q. Chen, L. Z. Feng, J. J. Liu, W. W. Zhu, Z. L. Dong, Y. F. Wu and Z. Liu, *Adv. Mater.*, 2016, **28**, 7129.

32 J. Kim, H. Y. Kim, S. Y. Song, S. H. Go, H. S. Sohn, S. Baik, M. Soh, K. Kim, D. Kim, H. C. Kim, N. Lee, B. S. Kim and T. Hyeon, *ACS Nano*, 2019, **13**, 3206–3217.

33 J. Karges, S. Kuang, F. Maschietto, O. Blacque, I. Ciofini, H. Chao and G. Gasser, *Nat. Commun.*, 2020, **11**, 3262.

34 H. G. Zhou, F. L. Qin and C. Y. Chen, *Adv. Healthcare Mater.*, 2021, **10**, 2001277.

35 J. Sun, X. T. Cai, C. J. Wang, K. Du, W. J. Chen, F. D. Feng and S. Wang, *J. Am. Chem. Soc.*, 2021, **143**, 868–878.

36 E. G. Ju, K. Dong, Z. W. Chen, Z. Liu, C. Q. Liu, Y. Y. Huang, Z. Z. Wang, F. Pu, J. S. Ren and X. G. Qu, *Angew. Chem., Int. Ed.*, 2016, **55**, 11467–11471.

37 X. S. Li, N. Kwon, T. Guo, Z. Liu and J. Yoon, *Angew. Chem., Int. Ed.*, 2018, **57**, 11522–11531.

38 C. Yao, W. X. Wang, P. Y. Wang, M. Y. Zhao, X. M. Li and F. Zhang, *Adv. Mater.*, 2018, **30**, 1704833.

39 S. Kuang, F. M. Wei, J. Karges, L. B. Ke, K. Xiong, X. X. Liao, G. Gasser, L. N. Ji and H. Chao, *J. Am. Chem. Soc.*, 2022, **144**, 4091–4101.

40 N. Kwon, H. Kim, X. S. Li and J. Yoon, *Chem. Sci.*, 2021, **12**, 7248–7268.

41 Y. F. Zhou, S. Y. Fan, L. L. Feng, X. L. Huang and X. Y. Chen, *Adv. Mater.*, 2021, **33**, 2104223.

42 B. J. Ma, S. Wang, F. Liu, S. Zhang, J. Z. Duan, Z. Li, Y. Kong, Y. H. Sang, H. Liu, W. B. Bu and L. L. Li, *J. Am. Chem. Soc.*, 2019, **141**, 849–857.

43 J. C. Yang, H. L. Yao, Y. D. Guo, B. W. Yang and J. L. Shi, *Angew. Chem., Int. Ed.*, 2022, **61**, e202200480.

44 F. Gong, N. L. Yang, Y. Wang, M. P. Zhuo, Q. Zhao, S. Wang, Y. G. Li, Z. Liu, Q. Chen and L. Cheng, *Small*, 2020, **16**, 2003496.

45 L. Z. Gao, J. Zhuang, L. Nie, J. B. Zhang, Y. Zhang, N. Gu, T. H. Wang, J. Feng, D. L. Yang, S. Perrett and X. Yan, *Nat. Nanotechnol.*, 2007, **2**, 577–583.

46 Y. Y. Ning, Y. Huo, H. Z. Xue, Y. J. Du, Y. H. Yao, A. C. Sedgwick, H. Y. Lin, C. C. Li, S. D. Jiang, B. W. Wang, S. Gao, L. Kang, J. L. Sessler and J. L. Zhang, *J. Am. Chem. Soc.*, 2020, **142**, 10219–10227.

47 C. Y. Cao, X. R. Wang, N. Yang, X. J. Song and X. C. Dong, *Chem. Sci.*, 2022, **13**, 863–889.

48 C. Zhang, W. B. Bu, D. L. Ni, S. J. Zhang, Q. Li, Z. W. Yao, J. W. Zhang, H. L. Yao, Z. Wang and J. L. Shi, *Angew. Chem., Int. Ed.*, 2016, **55**, 2101–2106.

49 N. Ferrara, H. P. Gerber and J. LeCouter, *Nat. Med.*, 2003, **9**, 669–676.

50 B. Li, Z. Gu, N. Kurniawan, W. Y. Chen and Z. P. Xu, *Adv. Mater.*, 2017, **29**, 1700373.

51 L. S. Lin, J. B. Song, L. Song, K. M. Ke, Y. J. Liu, Z. J. Zhou, Z. Y. Shen, J. Li, Z. Yang, W. Tang, G. Niu, H. H. Yang and X. Y. Chen, *Angew. Chem., Int. Ed.*, 2018, **57**, 4902–4906.

52 M. J. Xuan and J. B. Li, *Natl. Sci. Rev.*, 2021, **8**, nwab051.

53 D. Gerald, E. Berra, Y. M. Frapart, D. A. Chan, A. J. Giaccia, D. Mansuy, J. Pouysségur, M. Yaniv and F. M. Grigoriou, *Cell*, 2004, **118**, 781–794.

54 S. Akine, S. J. Piao, M. Miyashita and T. Nabeshima, *Tetrahedron Lett*, 2013, **54**, 6541–6544.

55 M. Y. Liu, Y. Y. Chu, H. Liu, Y. Q. Su, Q. Zhang, J. Jiao, M. Q. Liu, J. Q. Ding, M. Liu, Y. W. Hu, Y. Y. Dai, R. P. Zhang, X. R. Liu, Y. H. Deng and Y. Z. Song, *Mol. Pharmaceut.*, 2020, **17**, 1059–1070.

56 C. Alvarez, D. H. Shin and G. S. Kwon, *Pharm. Res.*, 2016, **33**, 2098–2106.

57 D. Becker, M. Klos and G. Kickelbick, *Inorg. Chem.*, 2019, **58**, 15021–15024.

58 M. L. Zhu, H. Zhang, G. Ran, D. N. Mangel, Y. H. Yao, R. Zhang, J. Tan, W. Zhang, J. Song, J. L. Sessler and J. L. Zhang, *J. Am. Chem. Soc.*, 2021, **143**, 7541–7552.

59 Y. Z. Zhang and H. Gorner, *Dyes Pigm.*, 2009, **83**, 174–179.

60 A. Antonio, F. M. Mario and A. Sandro, *Oxid. Med. Cell. Longev.*, 2014, 360438.

61 A. Yaghmur, B. Sartori and M. Rappolt, *Langmuir*, 2012, **28**, 10105–10119.

62 Y. X. Hou, Q. Fu, Y. F. Kuang, L. Di, Y. X. Sun, Z. Qian, Z. G. He and J. Sun, *J. Controlled Release*, 2021, **334**, 213–223.

63 T. C. Chou, *Cancer Res*, 2010, **70**, 440–446.

64 Z. S. Yang, Y. H. Yao, C. A. C. Sedgwick, C. Li, Y. Xia, Y. Wang, L. Kang, H. M. Su, B. W. Wang, S. Gao, J. L. Sessler and J. L. Zhang, *Chem. Sci.*, 2020, **11**, 8204–8213.

65 X. L. Guo, F. Liu, J. Deng, P. P. Dai, Y. Qin, Z. Li, B. B. Wang, A. P. Fan, Z. Wang and Y. J. Zhao, *ACS Nano*, 2020, **14**, 14715–14730.

66 S. W. Yu, H. Wang, M. F. Poitras, C. Coombs, W. J. Bowers, H. J. Federoff, G. G. Poirier, T. M. Dawson and V. L. Dawson, *Science*, 2002, **297**, 259–263.

67 G. L. Semenza, Targeting HIF-1 for cancer therapy, *Nat. Rev. Cancer*, 2003, **3**, 721–732.

68 D. Dong, Y. Fu, F. Chen, J. Zhang, H. Jia, J. Li, H. Wang and J. Wen, *Mol. Med. Rep.*, 2021, **23**, 62.

69 C. T. Ng, L. Y. Fong, J. J. Tan, N. F. Rajab, F. Abas, K. Shaari, K. M. Chan, F. Juliana and Y. K. Yong, *BMC Complement. Altern. Med.*, 2018, **18**, 210.

70 T. Xiang, Y. X. Lin, W. Ma, H. J. Zhang, K. M. Chen, G. P. He, X. Zhang, M. Xu, Q. S. Feng, M. Y. Chen, M. S. Zeng, Y. X. Zeng and L. Feng, *Nat. Commun.*, 2018, **9**, 5009.

71 S. Xu, A. N. Butkevich, R. Yamada, Y. Zhou, B. Debnath, R. Duncan, E. Zandi, N. A. Petasis and N. Neamati, *Proc. Natl. Acad. Sci. USA*, 2012, **109**, 16348–16353.

72 J. Wang, Q. Qi, W. Zhou, Z. Feng, B. Huang, A. Chen, D. Zhang, W. Li, Q. Zhang, Z. Jiang, R. Bjerkvig, L. Prestegarden, F. Thorsen, X. Wang, X. Li and J. Wang, *Autophagy*, 2018, **14**, 2007–2022.

73 X. S. Ke, J. Tang, J. J. Chen, Z. Y. Zhou and J. L. Zhang, *ChemPlusChem*, 2015, **80**, 237–252.